Land-cloud-climate coupling on the Canadian Prairies

Alan Betts, Atmospheric Research, Pittsford, VT, USA

Abstract: This is a review of a series of papers analyzing the long-term climate data from the Canadian Prairies, which show the coupling of the diurnal cycle of temperature and humidity to opaque cloud, snow cover, land-use, warm season precipitation and surface wind.

Keywords: Hydrometeorology, land-surface, cloud radiative forcing, snow cover, surface albedo, diurnal cycle, land-use

Introduction

Much of the conceptual analysis discussed in the previous chapter was based on reanalysis data, where we have the full suite of model variables. We included some discussion of some observational data from land-surface field programs. We now shift from the global model world to the climate of the real world at northern latitudes. This observational perspective of land-surface-cloud-atmosphere coupling uses the excellent climate station data from the Canadian Prairies, which is transforming our understanding of land-atmosphere coupling and more broadly hydrometeorology (Betts et al. 2013a, b; 2014a, b; 2015; Betts and Tawfik 2015). This is because, in addition to standard climate variables of high quality, there is a remarkable set of hourly observations of opaque or reflective cloud cover in tenths, made by trained observers who have followed the same protocol for 60 years (MANOBS 2013). Opaque cloud is defined as cloud that obscures the sun, moon or stars. These opaque cloud observations are sufficiently good that daily means can be calibrated against multiyear shortwave and longwave radiation data to give the shortwave and longwave cloud forcing (SWCF, LWCF). Historically many climate and hydrometeorology studies have been largely based on temperature and precipitation for which long-term records are available. Now perhaps for the first time, we have a full set of observational data, temperature, humidity, precipitation, cloud and radiation, and snow depth, to describe the fully coupled land-surface system. This chapter extracts material from these cited papers.

Major qualitative and quantitative advances in our understanding have emerged. On an annual timescale, it is clear that a high albedo snow cover acts as a fast climate switch, which drops the near-surface temperature by 10K; and at the same time transforms the surface-cloud coupling from an unstable boundary layer (BL), controlled by SWCF with no snow, to a stable BL controlled by LWCF with snow cover. In the warm season with no snow, we are able describe quantitatively the fully coupled system of temperature, humidity (and the derived thermodynamic variables), precipitation and cloud/radiation on daily, monthly and seasonal timescales, as well as see the impact of surface windspeed and RH.

Data sets and processing

Climate station data

Figure 1 shows the location of the 15 climate stations, Canadian ecozones, regional zones, agricultural regions and boreal forest. These have hourly data, starting in 1953 for all stations except Regina and Moose Jaw which start in 1954, and Edmonton which starts in 1961. The stations are all at airports. Most of the stations are in agricultural regions; while The Pas, Prince Albert and Grand Prairie are either in or close to the boreal forest. For the first four decades, these hourly data sets are essentially complete. In recent years, cutbacks have introduced gaps in the data at some stations. For example, Portage-Southport was the first to stop hourly observations on July 1, 1992 and go to only daytime observations, five days a week. Moose Jaw dropped night-time observations after July 1998, and Lethbridge and Medicine Hat dropped night-time observations in April 2006. At the time of processing in 2012, the datasets ran until the summer of 2011.

Daily climate data set.

The hourly climate variables include air pressure (p), dry bulb temperature (T), relative humidity (RH), wind speed and direction, total opaque cloud amount and total cloud amount. Most stations have cloud height data and low cloud amount. We generated a file of daily means for all variables, such as mean temperature and humidity, T_m, and RH_m; and extracted and appended to each daily record the corresponding hourly data at the times of maximum and minimum temperature (T_x and T_n). We merged a file of daily total precipitation and daily snow depth. This is our daily climate data set. Four stations, Lethbridge, Swift Current, The Pas and Winnipeg, have downward shortwave radiation SW_{dn} for some of the period. There was a Baseline Surface Radiation Network (BSRN) site measuring SW_{dn} and LW_{dn}, 25km south of Regina for the years 1995-2011.

Figure 1. Climate station locations, Canadian ecozones, regional zones, agricultural regions and boreal forest. *(Betts et al. 2013b)*

Since occasional hourly data were missing, we kept a count of the number of measurement hours, MeasHr, of valid data in the daily mean. Generally we have filtered out all days for which MeasHr <20, There are few missing hours of data in the first four decades, but this filter removes recent periods with only daytime data. From the hourly data we compute the diurnal temperature range between maximum temperature, T_x, and minimum temperature, T_n, as

$$DTR = T_x - T_n \qquad (1)$$

We also define the difference of relative humidity, RH, between T_n and T_x, as

$$\Delta RH = RH_{tn} - RH_{tx} \approx RH_x - RH_n \qquad (2)$$

where RH_x, RH_n are the maximum and minimum RH. This approximation is excellent in the warm season (but not the cold season), when surface heating couples with a convective BL. Then typically RH reaches a maximum near sunrise at T_n and a minimum at the time of the afternoon T_x . We also derived from p, T_x and RH_{tx}, the lifting condensation level (LCL), the pressure height to the LCL, P_{LCLtx}, mixing ratio (Q_{tx}) and θ_{Etx}, all at the time of the maximum temperature.

The effective cloud albedo is a scaled shortwave cloud forcing, SWCF

$$ECA = - SWCF/SWC_{dn} \qquad (3)$$

where $$SWCF = SW_{dn} - SWC_{dn} \qquad (4a)$$

and SW_{dn}, SWC_{dn} are the downward all-sky and clear sky fluxes. Note that ECA is the same whether it is defined in terms of the downward or net SW fluxes. Similarly for the longwave downward flux, we can define the LW cloud forcing

$$LWCF = LW_{dn} - LWC_{dn} \qquad (4b)$$

The total cloud forcing CF = SWCF+LWCF and the net cloud forcing $CF_n = (1- \alpha_{surf})CF$, where the surface albedo, $\alpha_{surf} \approx 0.7$ with surface snow cover and ≈ 0.2 with no snow cover.

Close neighbor comparison of opaque cloud data

We assessed the quality of the opaque/reflective cloud data made by trained observers across the Prairies over many decades (Betts and Tawfik 2015, submitted). Figure 2 compares daily mean opaque cloud for three neighboring pairs: Regina and Moose Jaw separated by 63km, Winnipeg and Portage-Southport, separated by 75 km, and Regina and Estevan, separated by 181km. The geometric mean slope of the regression of y on x and x on y are close to unity, showing that these daily means estimated by independent observers appear to be unbiased, and that daily mean cloud data at one station is spatially representative for distances of order 100km. This is not surprising as the 24h advection distance at 3.5 m/s is 300km. In fact, the geometric mean slopes of the opaque cloud regressions for each of these station pairs are close to unity out to the spacing of 250 km, although the correlation falls (not shown).

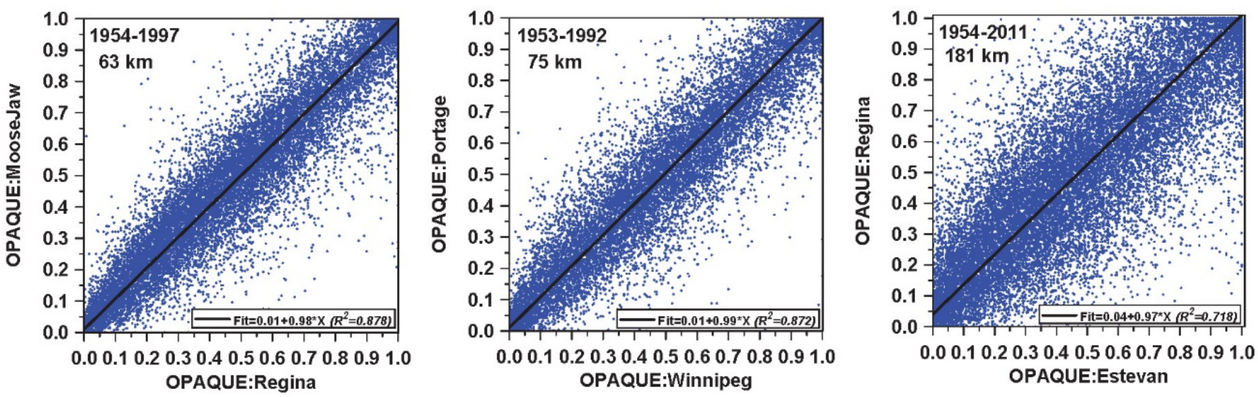

Figure 2. Comparison of daily mean opaque cloud cover for Moose Jaw and Regina for 1954-1997 (left); (center) Portage-Southport and Winnipeg for 1953-1992, and (right) Regina and Estevan for 1954-2011. *(Betts and Tawfik 2015)*

Annual diurnal cycles of opaque cloud

Figure 3 shows the annual cycle of the diurnal cycle of total and lowest-level opaque cloud cover averaged across all the climate stations. Two stations (Moose Jaw and Regina) have no lowest-level cloud observations. It is clear that, compared to winter, the summer months, especially July-August, generally have less cloud cover. This signature is seen in both the total and lowest-level cloud cover (upper panels). To remove the strong annual cycle and highlight the time of day of maximum and minimum cloud cover, each month is normalized by its maximum cloud cover and scaled where the minimum is zero and the maximum equals one (lower panels). This shows a clear shift in the time of day of maximum opaque cloud cover between cold and warm seasons. There is a morning (6 to 9 LST) maximum in total opaque cloud from November through March, and an afternoon (14 to 16 LST) maximum during the warm months, May through September (lower left). April and October are transition months. This separation of these diurnal maxima is sharper in the lowest-level cloud field (lower right). The morning maximum in low cloud, which is dominant in the cold season, is close to or a little before the minimum temperature near sunrise, which varies seasonally. The warm season afternoon low cloud maximum is about an hour ahead of the afternoon temperature maximum at 15 LST (see next section). Betts et al. (2014a, 2015) identified a sharp warm/cold regime change, which they attributed to a "fast" radiative switch corresponding to whether snow was present on the ground. However we see that for the transition month of October, which is before significant snowfall at many stations, the morning and afternoon maxima in total opaque cloud are both present (bottom left). However the afternoon maximum of low cloud found from April to September is no longer present (bottom right).

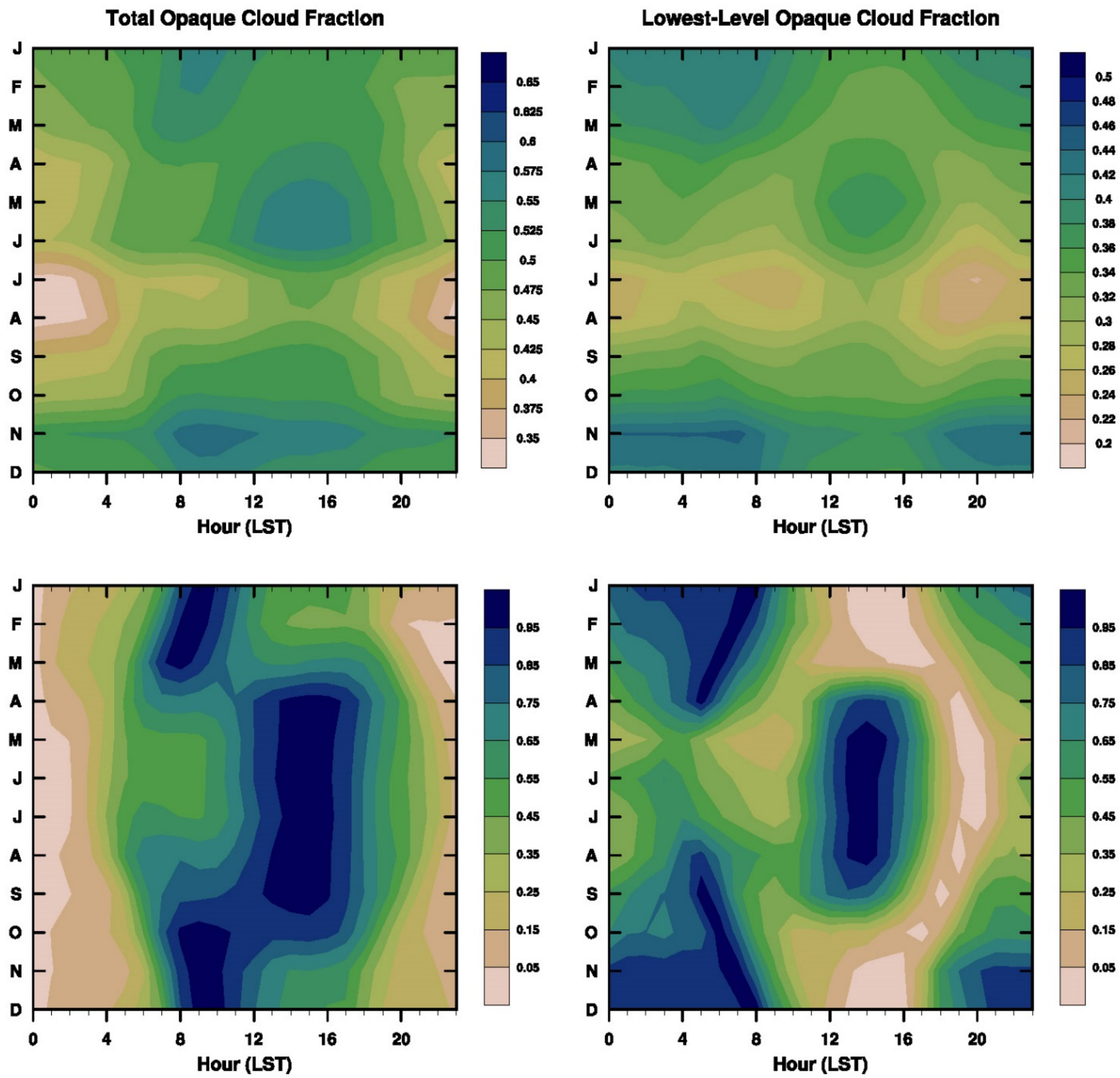

Figure 3. The average diurnal cycle of total opaque cloud fraction and lowest-level opaque cloud fraction over the annual cycle (top), and (below) the normalized diurnal cycles of total opaque cloud cover fraction and lowest-level opaque cloud fraction, scaled so that 1 is the diurnal maximum and 0 is the minimum. *(Betts and Tawfik 2015)*

Mean Annual Cycle of Cloud Forcing

We used the SW_{dn} and LW_{dn} data from the BSRN station at Bratts Lake, 25 km south of Regina, to calculate SWCF and LWCF. For the downward clear-sky fluxes (SWC_{dn} and LWC_{dn}), we started with the values computed for the nearest grid-point by the ERA-Interim reanalysis (ERI). We used LWC_{dn} from ERI as these appeared unbiased in comparison with BSRN data on clear days. However on these same clear days, the BSRN measured clear sky fluxes were greater than the computed ERI SWC_{dn}, so we derived a corrected fit (Betts et al. 2015) to the annual cycle.

$$SWC_{dn}(\text{fit}) = 65 + 310\ (\text{SIN}(\pi\ \text{DS} / 365))^{1.92} \qquad (5)$$

where DS = DOY + 14 for DOY < 351, and DOY - 351 for DOY >350 (adjusted for leap years).

Figure 4 shows the mean annual cycle of SWCF, LWCF, CF and CF_n, binned in 0.1 ranges of ECA for 1995-2011. There is a single bin for all the data for which ECA>0.7, and the standard error of the bin means is shown. The top left panel just shows the variation of SWCF with ECA, which follows directly from the definition (3). This shows that that the reduction of the surface SW flux by clouds is naturally largest in summer, when SWC_{dn} is largest. The sharp drop in reflective cloud cover between June and July (Betts et al., 2014b) gives the jump in the monthly mean for all data (heavy black curve).

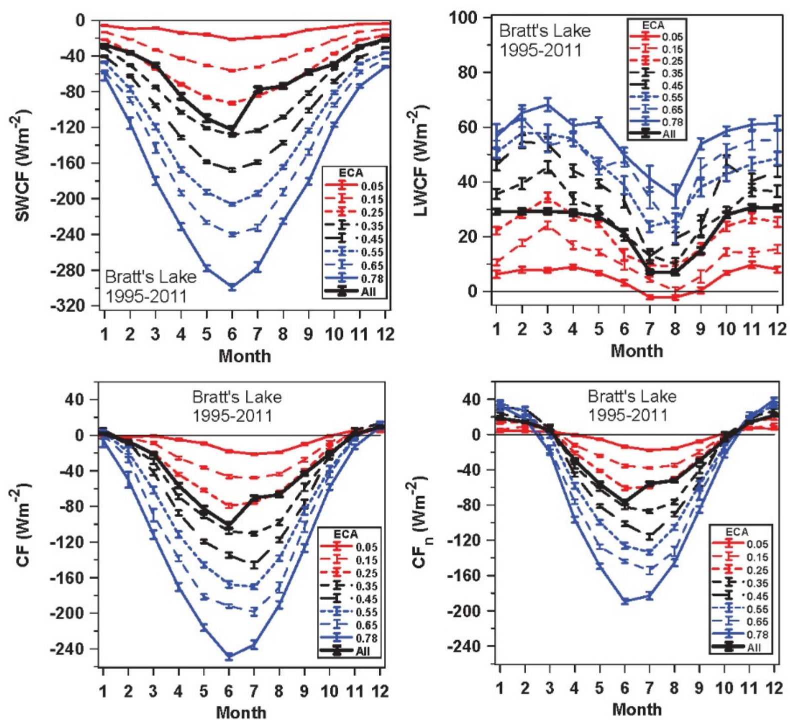

Figure 4. Mean annual cycle of SWCF, LWCF, CF and CF_n, stratified by ECA *(Betts et al. 2015)*

The top right panel shows that the LWCF increases with ECA. The impact of clouds on the LWCF is larger in winter than in summer, when the moister atmosphere is itself more opaque to LW radiation. The very small negative values in summer for ECA=0.05 may reflect a small positive bias in LWC_{dn} from ERA-Interim.

The bottom left panel is the sum of the upper two, which shows that the total cloud forcing of the down-welling flux is near zero from November to January, when SWC_{dn} is smallest. The bottom right panel is CF_n, the cloud forcing of the net surface radiative flux. For consistency with our 1995-2011 analysis period, we used monthly mean values of surface albedo from ERA-Interim, although the annual range from 0.19 in summer to 0.61 in winter is slightly less than the range of 0.16 to 0.73, shown in Betts et al. (2014a) for Saskatchewan for the 2000-2001 winter. The impact of reflective snow cover in reducing the net SW fluxes means that CF_n becomes positive from November to February (Betts et al., 2013). This reversal of the sign of CF_n leads to the two distinct climate states in the Canadian Prairies for the warm and cold seasons (Betts et al., 2014a).

Calibrating opaque cloud data at Regina to SWCF, ECA and LW_n using BSRN data

The climate station at Regina airport is about 25km north of the Baseline Surface Radiation Network (BSRN) station at Bratt's Lake, which has well-calibrated BSRN SW_{dn} and LW_{dn} observations for 1995-2011. We saw in Figure 2 that the daily mean, $OPAQ_m$, is representative of scales larger than this, so it reasonable to use the BSRN data to calibrate daily mean $OPAQ_m$ against daily mean LW_n. Since the daily mean SWCF and ECA in (3) depend only on daytime SW reflection and absorption, we defined a daily SW-weighted OPAQSW as a weighted sum of hourly OPAQ values during daylight hours, using weights derived from ERI clear-sky flux data (Betts et al. 2015). We found significant differences between warm and cold seasons, which were well separated by sub-setting the data by daily mean temperature T_m < > 0°C.

Figure 8 (left) shows the relation between ECA derived from the BSRN data and OPAQSW, for the warm season above freezing and the cold season below freezing. ECA increases more steeply with increasing opaque cloud in the warm season than the cold season. This division is very similar if we split by the months AMJJASO and NDJFM (not shown). We show the mean and standard error of the binned data, and the quadratic regression fits to the daily data. The uncertainty in ECA on a daily basis is of the order of ±0.08 in the warm season and ±0.11 in the cold season. The standard errors shown for the climatological fits are much smaller because they are reduced by the large number of days.

Figure 8 (middle) shows the dependence of LW_n, on opaque cloud and RH_m (taken from Regina because RH was not measured at Bratt's Lake for the first 5 years) for days above freezing (3245 days). Increasing atmospheric humidity reduces the outgoing LW_n flux for the same cloud cover. The temperature dependence is very small when T_m>0^{o}C (not shown). In contrast for temperatures below freezing (2198 days), the humidity dependence is small but the temperature dependence is large, shown in the right panel. The outgoing LW_n flux now decreases with colder temperatures, probably because the surface cools under a stable BL in the cold season (Betts et al., 2014a). Regression fits to the daily data (Betts et al. 2015) show that $OPAQ_m$, a daily mean calculated from the hourly observations of opaque cloud fraction by trained observers, together with daily mean temperature, humidity and TCWV in winter, gives daily mean LW_n to about ±9 W/m^2.

Net radiation is given by

$$R_n = SW_n + LW_n = (1- \alpha_{surf})(1\text{-}ECA)SWC_{dn} + LW_n \qquad (6)$$

Given opaque cloud cover, T_m and RH_m at climate stations, we can use the fits for ECA and for LW_n to estimate the climatological dependence of SW_n, LW_n and R_n.

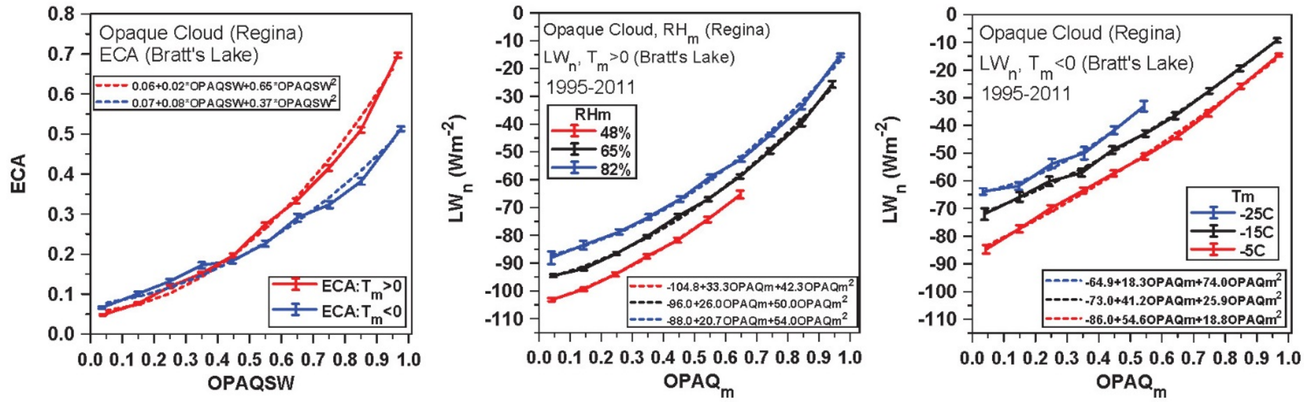

Figure 5. Relation between Opaque cloud at Regina and Bratt's Lake ECA (left), LW_n and stratified by RH_m in warm season (middle) and (right) LW_n stratified by T_m in cold season. *(Betts et al. 2015)*

Warm and cold climates in the Prairies

There are two primary Prairie climates, sharply separated by the freezing point of water: one for the warm season without snow, and one for the cold season with reflective surface snow. Snow cover acts as a climate switch, which changes the sign of the net cloud forcing (Figure 4). Figure 6 shows the stratification by opaque cloud for these two regimes. There is a smaller group (Betts and Tawfik 2015), when it is below freezing but there is no snow cover, or it is above freezing but not all the snow has melted (not shown).

The upper panels are the warm season class (141,160 days), stratified by $OPAQ_m$. T_n at sunrise barely changes with opaque cloud, but afternoon T_x (and T_m) increase as cloud cover decreases. This warm regime is SWCF dominated, characterized by a growing unstable convective BL in the daytime (Betts et al., 2015), and the coolest temperatures under cloudy skies, when 69% of the days have >1mm of precipitation (Betts and Tawfik 2015). The strong diurnal cycle for the warm regime has a minimum in RH (top center) corresponding to a maximum of P_{LCL} in the afternoon at the temperature maximum. The diurnal cycle of mixing ratio, Q, (top right) is quite different. For $OPAQ_m$<0.7 it shows morning and evening peaks in Q with minima near sunrise and in the mid-afternoon. This is the characteristic signal of an unstable growing daytime BL, which couples and uncouples to a deeper BL above (Betts et al. (2013a). After sunrise, evaporation is trapped for some hours in the shallow night-time BL, warming and moistening the near-surface air after the sunrise Q minimum. Around 10 LST, the growing BL recouples with a deep residual BL, and Q falls to an afternoon minimum as the growing BL entrains drier air from above. After the time of maximum temperature, the near-surface layer again decouples, and Q rises until sunset when evapotranspiration drops to very low values. Betts et al. (2013a) showed that the calculated LCL corresponded to the height of the lowest cloud-base in summer.

The lower panels are the cold season class (74260 days), where the average snow depth is 17.2(±0.7) cm, and there is typically a stable BL. The coupling of the diurnal cycle of temperature to $OPAQ_m$ is quite different from the warm season because LWCF dominates (Figure 4). It is warmest when it is cloudy, but as cloud cover decreases, T_n at sunrise falls steeply, as does T_m. We see that the diurnal range of temperature is largest under nearly-clear skies, when the daytime solar forcing is largest, but despite this T_x still increases with $OPAQ_m$. For the cold regime, RH and Q drop with decreasing opaque cloud cover and they show only single minima and maxima in the afternoon.

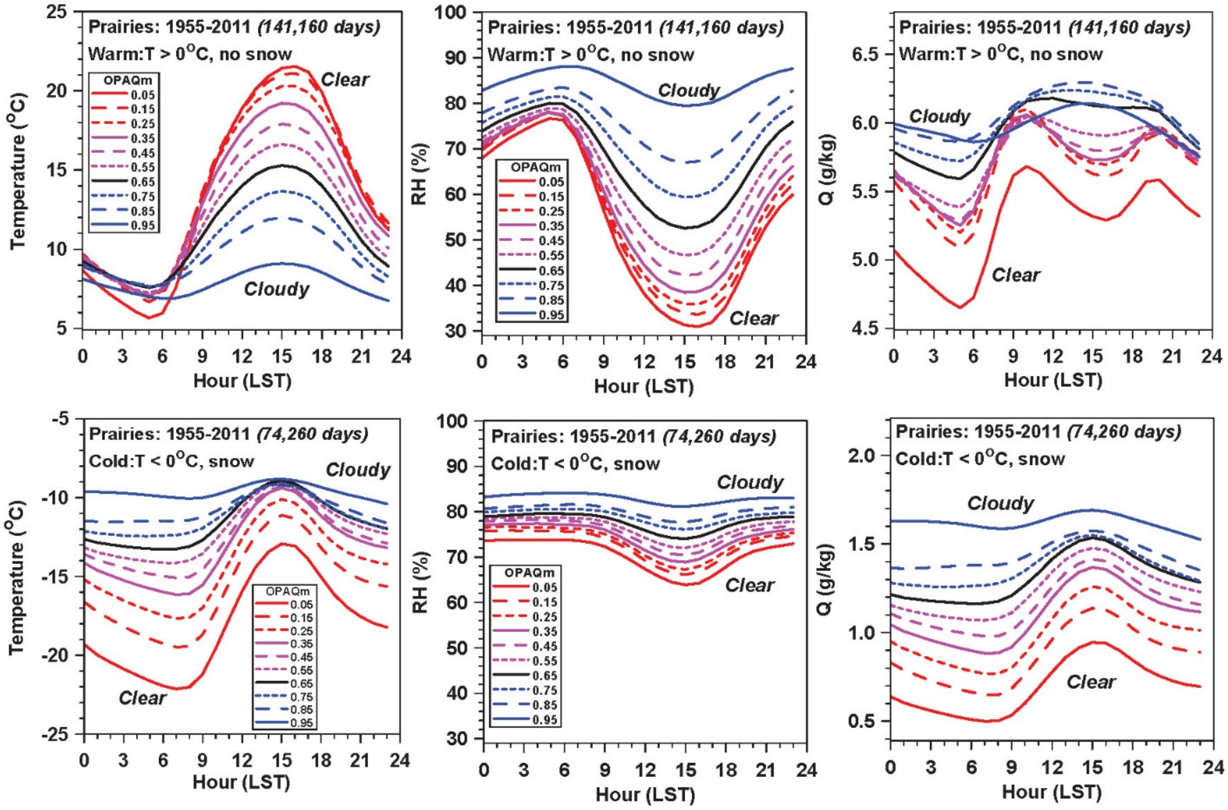

Figure 6. Diurnal cycle of temperature, RH and mixing ratio Q, stratified by $OPAQ_m$ for warm season (top) and (bottom) cold season with snow cover. *(adapted from Betts and Tawfik 2015)*

Coupling of snow to surface climate

The fast local climate response can be seen if we can map the transitions temporally across the snow boundaries (Betts et al. 2014a). Figure 7 (left panels) composites the climate station data with respect to days from fresh snowfall in the fall and the final melt of the snow pack in spring for six stations in Saskatchewan over 50 years. November 15 is the mean date of first snowfall that is not transient, and March 26 is the average date of final snowmelt. We see daily mean temperature falls by 10°C in about a week with first snowfall, and rises a little more slowly by the same amount in spring as the snowpack melts. This fast transition in the local climate with fresh surface snow was described by Betts et al. (2014a) as a climate switch, driven by two radiative processes. They estimated that the large increase in the surface albedo with snow cover reduced SW_n by 34 W/m^2, and reduced LW_{dn} by 15W/m^2, perhaps associated with both the stable BL, and a reduction in atmospheric water vapor with surface ice. The combined reduction of 49 W/m^2 is sufficient to produce an equilibrium 11K drop in radiative skin temperature.

In Alberta in the lee of the Rocky Mountains the winter snowpack is often transient, in part because of chinook winds. Figure 7 (right panel) plots mean temperature for the period October to April, when snow may occur on the Canadian Prairies, against the fraction of days with snow cover for five Alberta stations, each with almost fifty years of data. The effect of snow cover as a fast climate switch is so strong that most of the interannual variation in the cold season average temperature depends simply on the fraction of days with snow cover. The temperature range of 14.6°C from zero to 100% snow cover is larger than the local change with snow cover in the fall and spring of 10°C. This separation between the cold and warm season, linked to the freezing point of water and the presence of surface snow is a fundamental characteristic of northern climates.

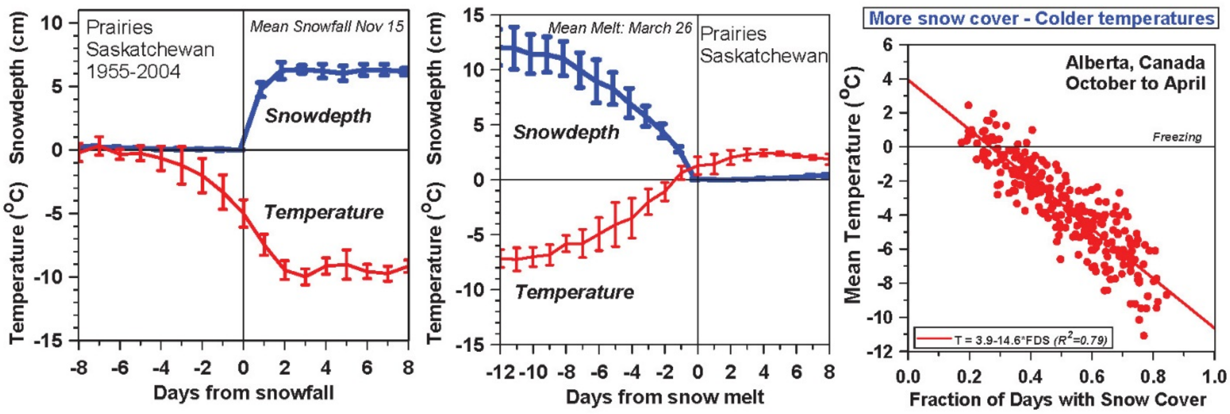

Figure 7. Change in mean temperature across surface snow cover transitions (left and center) and (right) *r*elation of mean October-April temperature to fraction of days with snow cover. *(Adapted from Betts et al. 2014a)*

Impact of land use change on diurnal climate

In the past thirty years there has been a major change in land use over the Canadian Prairies, specifically the conversion of more than five million hectares of summerfallow, (where the land was left bare for one year), to continuous cropping. The large increase in the area of cropland has increased summer transpiration, which has modified the growing season climate over the Prairies (Gameda et al., 2007). There has been a decrease in mean daily maximum temperature and the diurnal temperature range, a small decrease in the incoming solar radiation, and a small increase in precipitation (Betts et al. 2013b).

Change in cropping

The ecodistrict crop data were interpolated and averaged in the 50km radius region centered on each climate station shown in Figure 1. The trends for Saskatchewan for cropland (red), pasture (green) and summerfallow (blue) around each climate station are shown in Figure 8, where the transition from summerfallow to cropland has been largest. In the 1960’s and 1970’s the summerfallow exceeded 30% of land area around Regina, Estevan and Swift Current, but since 1991 this has fallen sharply to a current value around 5%. To assess the impact of land use change, we split the timeseries into two periods: a historic period, 1954-1991, when summerfallow cover was large and a recent period, 1992-2011, as summerfallow has fallen rapidly.

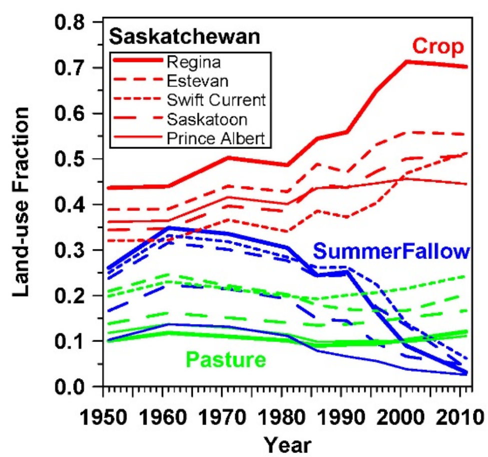

Figure 8. Long term trends in total cropland, pasture, and summerfallow around five climate stations in Saskatchewan

Mean change in the annual cycle in Saskatchewan

Figure 9 (left and center panels) shows the difference of the annual cycles for the mean of three stations, Saskatoon, Regina and Estevan in Saskatchewan, for which the datasets are complete for the whole time period. The data are 10-day means of the daily data (Betts et al., 2013b), plotted as Day of Year (DOY). The left panel shows the mean changes in the annual cycle of DTR, T_x, T_m and T_n and the center panel the mean changes in RH_m, ΔRH and opaque cloud (Betts et al. 2013b). The right panel is discussed below. We show four dotted lines to visually link the changes in different variables at DOY= 135, 195, 235, and 280, corresponding to May 15, July 14, August 23 and October 7. Some winter warming is visible between the two time-periods, but otherwise DTR, RH_m and ΔRH show no systematic differences in the cold season. Agricultural land-use has little impact when snow covers the ground.

There are two spring transitions [*Betts* 2011a]. The first is the sharp transition after DOY=85 (March 26), which is the average date of snowmelt [*Betts et al.* 2013a], when there is a sharp rise of DTR and ΔRH and a fall of RH_m. The diurnal cycle of temperature and RH change from a cold season to a warm season state (Betts et al. 2013a). The soil then dries, and with the solar zenith angle decreasing rapidly, temperature rises and humidity falls to a minimum. RH_m reaches a climatic minimum about 5-6 weeks after snowmelt. The peak in DTR and minimum in RH_m around DOY=135 (May 15) mark the beginning of the second spring transition that occurs with the green-up of the landscape and the spring growth of annual crops (Schwartz and Karl 1990; Schwartz 1994, 1996). In the recent period the peaks in DTR and trough in RH_m are earlier by 10-20 days. This is consistent with the earlier start to the growing season by several days per decade (Qian et al. 2009, 2011). However, this transition depends on the planting dates of annual crops, as well as the impact of a warming winter climate on the spring regrowth of perennial crops and the natural ecosystem.

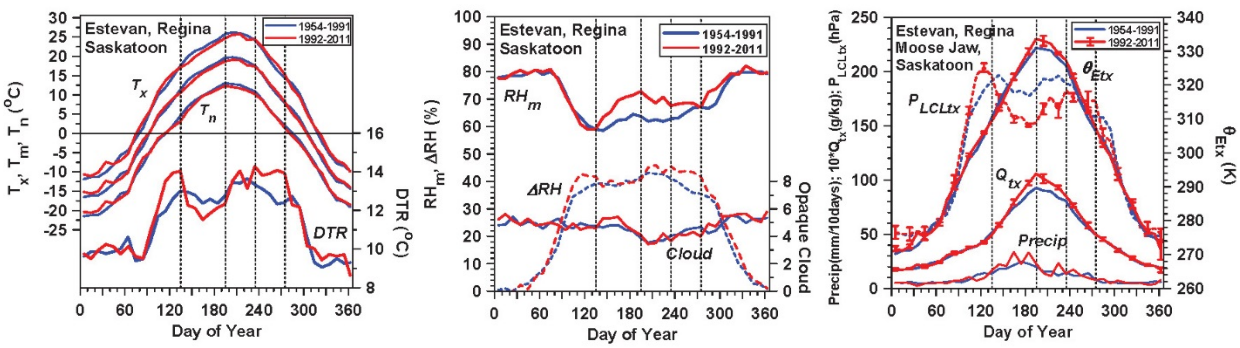

Figure 9. Mean change in annual cycle of T_x, T_m, T_n and DTR (left); (center) RH_m, ΔRH and opaque cloud for Saskatoon, Regina and Estevan and (right).

The change in the seasonal cycle from the early (mean of 1972) to later period (mean of 2001) has these characteristics:

1) For 140≤DOY<200 (May 20-July 18), the recent period has a DTR that is lower by -0.6 ºC, with T_x lower by -1.2 ºC and T_n lower by -0.6 ºC.

2) For 140≤DOY<240 (May 20-August 27), RH_m averages 7% higher in the recent period, and reaches a peak at DOY=195 (July 14).

3) For 140≤DOY<200 (May 20-July 18), mean opaque cloud is higher by 0.4 tenths on average in the recent period, and precipitation has increased 24%.

Figure 9 (right panel) shows the change in θ_{Etx} and P_{LCLtx}, Q_{tx}, at the afternoon maximum temperature; as well as the change in daily precipitation, for the mean of four Saskatchewan stations. Moose Jaw has been added because it has precipitation data (1954-2011) as well as daytime data at the time of T_x. The standard deviations shown on the 1992-2011 mean curve are for the differences across the four stations between the two time periods. The impact of the change in land-use is visible during the growing season. In the recent period from 1992-2011, the higher RH_{tx} over the Prairies from increased evapotranspiration gives P_{LCLtx} that is lower by 24 hPa for 140≤DOY<240; and for 160≤DOY<260 gives θ_{Etx} that is higher by 1.8K, and Q_{tx} that is higher by 9.4%. Precipitation over the Prairies in recent decades has increased, especially from June 15-July 15 (166≤DOY<196) during the period of peak crop transpiration (Gameda *et al.* 2007). Precipitation is a noisy variable, but Figure 9 shows a mean precipitation increase of 24% in the early growing season (140≤DOY<200), coincident with the fall of P_{LCLtx}. This suggests that local evaporation-precipitation feedback may be increasing precipitation. Almost all summer days have low-level boundary layer cloud, so P_{LCL} generally corresponds to the pressure-height of cloud-base. A lower cloud-base and higher θ_E, favors deep convection, and an increase of Q for air lifted to cloud-base is consistent with an increase in precipitation. De Ridder (1997) showed that θ_E generally increases with increasing evaporative fraction, which increases the potential for precipitating convection. Raddatz (1998) also suggested that increased ET during the height of the growing season, which enhances the potential for moist deep convection, is likely to have resulted in more frequent and severe precipitation events. Raddatz and Cummine (2003) have suggested there is a link between increased ET from the agro-ecosystem, increased boundary layer moisture and the number of tornado days over the Prairies.

One historic reason for summerfallow was to reduce ET and conserve soil water in a dry climate. However the increase of ET from the conversion to cropland may have increased precipitation. This near balance in summer between ET and precipitation over northern continental regions, including Canada, has been seen in global model simulations over a wide range of initial soil moisture conditions (Betts 2004). For the Prairies, Wang et al. (2013) show that there is a close balance between precipitation and ET over the annual cycle. We conclude that more intensive agriculture has increased transpiration, which has cooled and moistened the growing season climate. An increase in daily precipitation is consistent with a lowered cloud-base, increased afternoon mixing ratio and equivalent potential temperature (Betts et al. 2013b).

Monthly and seasonal warm season land-surface coupling

Monthly and longer timescales are clearly of importance to the understanding of both the impact of climate on agriculture and agriculture on climate. The key landscape contribution to climate in the warm season is the transpiration and evaporation of water, which depends on vegetation phenology and soil water. The climate station data have neither soil water measurements nor measurements of the surface fluxes. However, using multiple linear regression, we can show that much of the monthly variance of the surface climate, represented by temperature, humidity and cloud-base is linked to anomalies of opaque cloud cover and precipitation, which have distinct roles in the energy and water budget (Betts et al. 2014b).

Historically hydrometeorology has been based largely on temperature and precipitation for which long-term observational records are generally available. Similarly, model analyses of climate change typically focus on temperature and precipitation, and it is thought that uncertainties in cloud processes explain much of the spread in modeled climate sensitivity (Flato et al., 2013; Berg et al., 2014). In contrast, the Canadian Prairie data have sixty years of hourly observations for the fully coupled system of temperature, RH, precipitation, and opaque cloud observations, from which daily radiation can be estimated (Betts et al. 2015).

Monthly regression statistics

Betts et al. (2014b) looked at the coupling of diurnal anomalies to opaque cloud (in tenths) and precipitation anomalies (in mm/day) on monthly and longer timescales, for 11 Prairie stations with precipitation. For each station and each month, we removed the station monthly means, and then merged the station anomalies. This gives about 585 station-years of data for each month. We calculated the linear regression fits for the warm season months May to October, for Y = T_x, DTR, RH_{tx}, P_{LCLtx} and other variables in the form

$$\delta Y = K + A*\delta Precip(Mo\text{-}2) + B*\delta Precip(Mo\text{-}1) + C*\delta Precip + D*\delta OpaqueCloud \qquad (7)$$

Regression showed memory of precipitation anomalies for two previous months, but only opaque cloud anomalies for the current month. Tables 1 and 2 show the regression coefficients for equation (7) for δDTR and δRH_{tx}.

Table 1. δDTR anomalies: equation (7)

Month	*K*	*A (Mo-2)*	*B(Mo-1)*	*C (Mo)*	*D (Mo)*	*R^2*
May	*0±0.8*		*-0.37±0.05*	*-0.37±0.04*	*-1.10±0.05*	*0.73*
Jun	*0±0.7*		*-0.30±0.03*	*-0.32±0.02*	*-0.97±0.04*	*0.69*
July	*0±0.7*	*-0.20±0.03*	*-0.25±0.02*	*-0.33±0.03*	*-1.10±0.05*	*0.67*
Aug	*0±0.7*	*-0.07±0.02*	*-0.21±0.03*	*-0.40±0.03*	*-1.24±0.04*	*0.79*
Sept	*0±0.8*		*-0.22±0.03*	*-0.49±0.04*	*-1.27±0.04*	*0.82*
Oct	*0±0.8*		*-0.27±0.03*	*-0.70±0.07*	*-1.33±0.04*	*0.77*

Source: Data adapted from Betts et al. (2014b)

Table 2. Afternoon δRH_{tx} anomalies: equation (7)

Month	*K*	*A (Mo-2)*	*B(Mo-1)*	*C (Mo)*	*D (Mo)*	*R^2*
May	*0±3.6*	*1.30±0.38*	*1.47±0.22*	*2.07±0.17*	*4.75±0.20*	*0.72*
Jun	*0±3.6*	*0.69±0.23*	*1.26±0.15*	*1.96±0.12*	*4.36±0.22*	*0.68*
July	*0±4.1*	*0.84±0.18*	*1.71±0.12*	*1.81±0.17*	*4.40±0.30*	*0.59*
Aug	*0±3.6*	*0.66±0.11*	*1.23±0.13*	*2.42±0.16*	*4.08±0.20*	*0.73*
Sept	*0±3.5*		*1.40±0.13*	*2.10±0.18*	*4.35±0.16*	*0.75*
Oct	*0±4.3*		*1.28±0.19*	*5.02±0.39*	*4.58±0.23*	*0.67*

Source: Data adapted from Betts et al. (2014b)

We have omitted values that do not contribute to the explained variance. We have highlighted August at the end of the growing season. The dependence of precipitation is largest for the current month and decreases for earlier months. There are many months when the contribution of δPrecip(Mo-2) is insignificant; more for DTR than for RH_{tx}. The explained variance is as high as 0.82 for DTR and 0.75 for RH_{tx} in September, but considerably lower in July at peak crop growth. Opaque cloud anomalies are the dominant contribution for DTR (not shown). For RH_{tx} the contribution from precipitation anomalies is comparable to that of opaque cloud for JJA, (not shown). It is clear that both opaque cloud (which determines R_n) and precipitation play crucial roles in determining the monthly climatology of land-surface coupling in the warm season. Note that the climate memory is not in the precipitation anomalies themselves. The 1-month lagged auto-correlation of precipitation anomalies, δPrecip on the preceding month δPrecip(Mo-1), for the 2341 growing season months (MJJA) has R^2 =0.000; so precipitation anomalies, δPrecip(Mo-2), δPrecip(Mo-1), δPrecip can be treated as independent. Models show that the memory is in soil moisture [*Koster and Suarez* 2001, *Beljaars et al.* 1996; *Betts* 2004].

Standardized regression for growing season anomalies

Betts et al. (2014b) generated averages for the growing season (May, June, July and August: MJJA). There are 580 years with complete MJJA data. For each station, they subtracted the station means, and looked at the multiple regression of temperature and humidity anomalies on MJJA opaque cloud and precipitation anomalies. In this 4-month average, the dependence on precipitation for the previous months are included, except for April precipitation anomalies. These were included by defining

$$\delta Precip(AMJJA) = 0.25*\delta Precip(April) + \delta Precip(MJJA) \quad (8)$$

The weighting factor of 0.25 on δPrecip(April) (in units of mm/day) comes from the reduced impact of a single month on the four-month mean. By dividing all variables by their standard deviation, σ, they found the standardized regression coefficients, shown in Table 3, for the relationship

$$\delta Y_\sigma = K_\sigma + B_\sigma*\delta Precip(AMJJA)_\sigma + C_\sigma*\delta OpaqueCloud_\sigma \quad (9)$$

The standard deviations are 0.614 mm/day for δPrecip(AMJJA) and 0.434 Tenths for δOpaqueCloud: for **δ**Y they are shown in the right column of Table 3. On the growing season timescale, precipitation and cloud variability is responsible for 50-60% of the variability of the standardized variables, $\boldsymbol{\delta T_{x\sigma}}$, $\boldsymbol{\delta DTR_\sigma}$, $\boldsymbol{\delta RH_{tx\sigma}}$, $\boldsymbol{\delta P_{LCLtx\sigma}}$, which are highlighted. In contrast, R^2 for $\boldsymbol{\delta T_{n\sigma}}$, is small, presumably because T_n, unlike T_x, DTR and RH_{tx}, has little dependence on opaque cloud (Figure 6). On this growing season timescale, we can see that while C_σ for opaque cloud anomalies is the dominant term for δT_x, δT_m, δT_n; in contrast B_σ for precipitation anomalies is the dominant term for δDTR, the δRH variables, as well as δP_{LCLtx} and δQ_{tx}. On the 50-year climate timescale, Betts et al. (2014b) found that the inter-station variability of DTR and δRH_{tx} depend only on precipitation, whereas the variability of δT_x depends only on cloud variability.

Table 3. Regression of growing season standardized climate anomalies on precipitation and opaque cloud standardized anomalies.

Variable: δY_σ	*K_σ*	*B_σ*	*C_σ*	*R^2_σ*	*$\sigma(\delta Y)$*
$\boldsymbol{\delta T_{x\sigma}}$	*0±0.7*	*-0.33±0.03*	*-0.52±0.03*	*0.52*	*1.11*
$\boldsymbol{\delta T_{m\sigma}}$	*0±0.8*	*-0.21±0.05*	*-0.50±0.07*	*0.38*	*0.88*
$\boldsymbol{\delta T_{n\sigma}}$	*0±1.0*	*0.11±0.04*	*-0.33±0.04*	*0.09*	*0.77*
$\boldsymbol{\delta DTR_\sigma}$	*0±0.6*	*-0.55±0.03*	*-0.39±0.03*	*0.62*	*0.83*
$\boldsymbol{\delta RH_{tx\sigma}}$	*0±0.6*	*0.56±0.03*	*0.35±0.03*	*0.60*	*4.35*
$\boldsymbol{\delta RH_{m\sigma}}$	*0±0.7*	*0.51±0.03*	*0.33±0.03*	*0.50*	*4.61*
$\boldsymbol{\delta RH_{tn\sigma}}$	*0±0.9*	*0.38±0.04*	*0.24±0.04*	*0.27*	*4.52*
$\boldsymbol{\delta \Delta RH_\sigma}$	*0±1.0*	*-0.24±0.04*	*-0.15±0.04*	*0.11*	*2.97*
$\boldsymbol{\delta P_{LCLtx\sigma}}$	*0±0.6*	*-0.56±0.03*	*-0.37±0.03*	*0.61*	*18.6*
$\boldsymbol{\delta Q_{tx\sigma}}$	*0±0.9*	*0.50±0.04*	*0.03±0.04*	*0.26*	*0.58*
$\boldsymbol{\delta \theta_{Etx\sigma}}$	*0±1.0*	*0.22±0.04*	*-0.31±0.04*	*0.09*	*1.95*

Source: Data adapted from Betts et al. (2014b)

Simplified water and energy balance for the growing season

Betts et al. (2014b) used a decade of data from the Gravity Recovery and Climate Experiment (GRACE) to estimate the coupling between the variability of precipitation and total water storage on the landscape. They found that the seasonal dry-down of total water storage damps 56% of the MJJA precipitation anomalies. Using this constraint on the water budget, and deriving the variability of R_n from the variability of opaque cloud, they showed how growing season anomalies of precipitation and opaque cloud cover are coupled to both the surface fluxes of sensible and latent heat, as well as the surface diurnal climate, represented by the observables DTR, T_x, RH_{tx} and P_{LCLtx}.

Figure 10 shows this simplified seasonal description of the fully coupled system. The left panel couples MJJA precipitation variability to the MJJA change in total water storage change (-ΔTWS), using the coupling coefficient F=0.56 derived from the GRACE analysis, and the mean seasonal drawdown of water storage (-ΔTWS_m). The evaporation E = P – R + (-ΔTWS), where we estimated R/P =0.05 (Betts et al. 2014b). We also show the corresponding latent heat flux λE. The center and right panels use the long-term climate coupling between opaque cloud and precipitation (δCloud = 0.73 δPrecipitation) to link R_n to cloud to precipitation. Given R_n, λE and ground storage G = 0.134 R_n from the ERA-Interim reanalysis, H can be found as a residual; and Bowen ratio (BR) and evaporative fraction (EF) can be calculated. We also used the regression relations from Table 3 to couple cloud and precipitation to the changes of DTR and RH_{tx} that are shown.

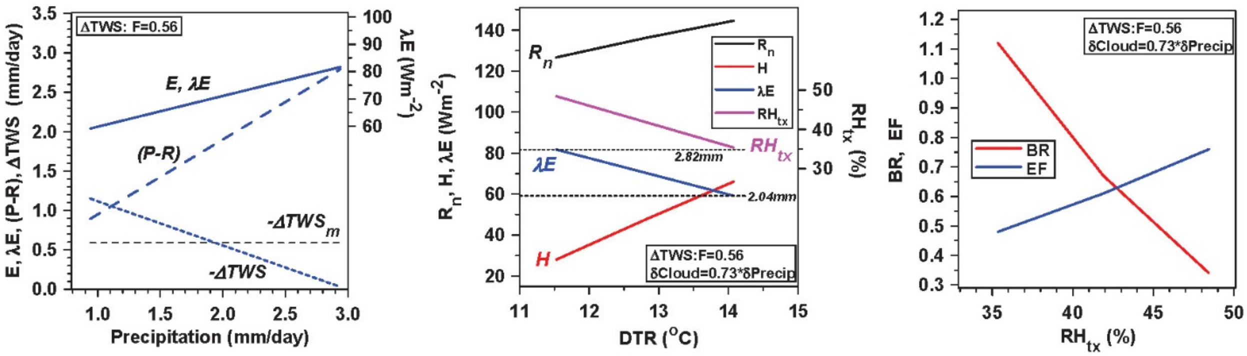

Figure 10. Growing season coupling of variability of cloud and precipitation to surface fluxes of energy and water and the surface diurnal climate *(from Betts et al. 2014b)*.

Daily time scale coupling in summer

This section shows the daily coupling in summer (JJA) as representative of the warm season. We have nearly 600 station-years of the Prairie data with opaque cloud observations, which we have calibrated to daily ECA and LW_n. There is sufficient data in the summer season (nearly 54000 days) to identify other processes that give a systematic daily climate signal in the fully coupled surface-BL-atmosphere system. Note that the data includes all the synoptic variability that is coupled to the diurnal cycle, but our sub-setting of this large dataset extracts the daily climate signal related to specific variables. We use $OPAQ_m$ as the primary stratification, available at all the Prairie climate stations, because of its tight coupling to LW_n and the diurnal cycle of temperature (Betts, 2006; Betts et al. 2015). Here we show just the sub-stratification by relative humidity and surface wind, and look at the coupling to radiation. Because of the large sample size the standard errors (SE) of the mean are small.

Dependence of daily summer climate on mean opaque cloud, partitioned by RH

Figure 11 shows the partition of the merged summer data (Betts et al. 2015), using $OPAQ_m$ and 5 ranges of mean RH_m (<50%, 50-60%, 60-70%, 70-80%, >80%). Note that the variability of RH_m in summer may come from both local processes, such as changes in surface evaporation related to soil moisture or vegetation phenology, as well as remote processes, such as synoptic advection. The left panel shows the mean structure (with SE uncertainty) for T_x, DTR and T_n, as well as daily precipitation, and the right panel shows Q_{tx} and θ_{Etx}. The magenta lines (small SE bars omitted for clarity) show the mean of the daily data, without the partition into bins of RH_m. For the mean data we see that T_x, DTR, and θ_E fall with increasing cloud cover, while T_n is almost flat, and Q_{tx} increases. Mean precipitation increases steeply at high opaque cloud cover.

The sub-partition into RH_m bins presents a different and interesting picture. The increasing size of the SE bars indicates fewer days in each bin, and we drop the mean once there are < 200 days in a bin. With a drier RH_m, T_x increases systematically, but T_n only increases for very dry conditions when RH_m <50%. Perhaps this is an indicator of drought. DTR however increases monotonically with decreasing RH_m. Figure 10 suggests that this change is probably coupled to decreasing evaporation. Precipitation becomes near-zero for days with RH_m < 50%, but is high for RH >80% and also increases with cloud cover. Q_{tx} now decreases with increasing opaque cloud cover in the higher RH_m bins, because of the steep fall of T_x with increasing cloud cover and precipitation. Although θ_{Etx} falls with increasing cloud cover, there is an upward shift to higher θ_{Etx} with increasing RH_m, which is also coupled to higher precipitation. Conversely, while T_x increases under dry conditions, we see this gives a fall of Q_{tx} and θ_{Etx} for the same cloud cover, and the lowest afternoon θ_{Etx} is associated with almost no precipitation.

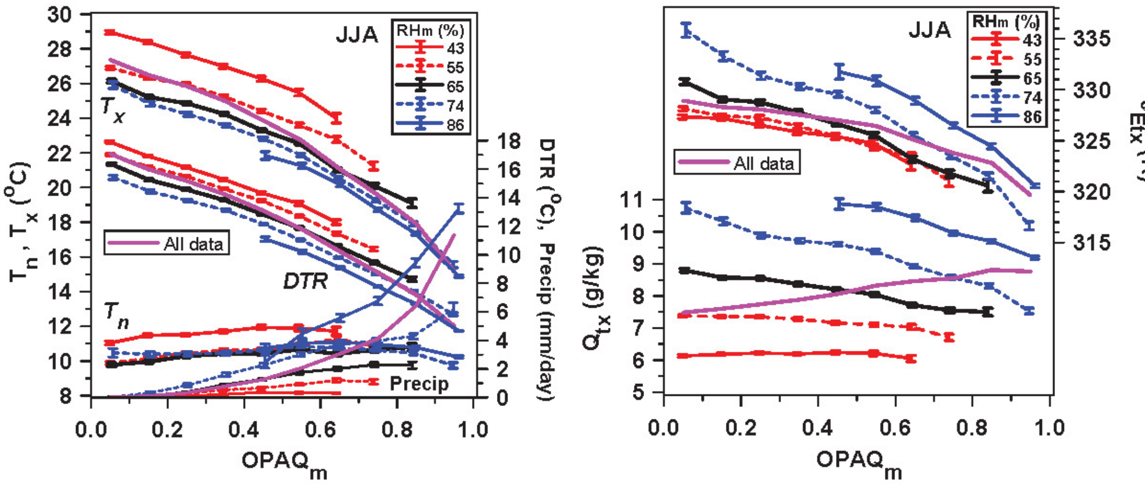

Figure 11: Coupling of $OPAQ_m$ and RH_m to precipitation and diurnal cycle of temperature (left) and (right) afternoon Q_{tx} and θ_{Etx} *(from Betts et al. 2015)*

Dependence of daily summer climate on cloud, partitioned by mean windspeed

Figure 12 shows the dependence of daily summer climate on opaque cloud, partitioned into four windspeed ranges (<2, 2-4, 4-6 and >6 m/s). Mean windspeed is 3.45 m/s. We see that the stratification by surface windspeed shows a climate signal in both the daytime and night-time near-surface layer. At low windspeed, afternoon T_x and RH_{tx} are slightly higher, corresponding to a substantial increase of Q_{tx} and θ_{Etx}. At sunrise under low cloud cover, T_n falls and RH_{tn} increases substantially with decreasing windspeed. These changes at T_n are a major contribution to the fall of the diurnal ranges of DTR and ΔRH with increasing windspeed. The cooling of T_n with decreasing windspeed at low $OPAQ_m$ is consistent with greater night-time cooling by outgoing LW_n and reduced wind stirring, increasing the stable stratification of the night-time BL (Betts 2006). Note there is a weak reversal at high cloud cover, when LW_n is small and the fall of surface T may be dominated by the evaporation of precipitation. The fall of RH_{tn} with increasing windspeed may be related to the mixing down of drier air.

At higher windspeeds in the afternoon, θ_{Etx} decreases with increasing cloud cover, presumably related to the reduction of the surface R_n with $OPAQ_m$, as well as the likelihood of low θ_E downdrafts at higher precipitation rates. However the small increases in T_x and RH_{tx} with decreasing windspeed lead to a broad maximum in θ_{Etx} for opaque cloud < 0.5, typical of a shallow cumulus field. An increase of maximum θ_E in summer suggests that there may be increased moist convective instability at low windspeeds during the growing season (De Ridder, 1997). Comparing the wind dependence of θ_{Etx} and precipitation with increasing cloud cover, we see that in summer there is a small indication that lower windpeed, higher θ_{Etx} and precipitation are coupled for $OPAQ_m$ < 0.8. However for $OPAQ_m$ = 0.95, there is a sharp increase of precipitation with windspeed, probably because the major rain events are associated with higher windspeeds.

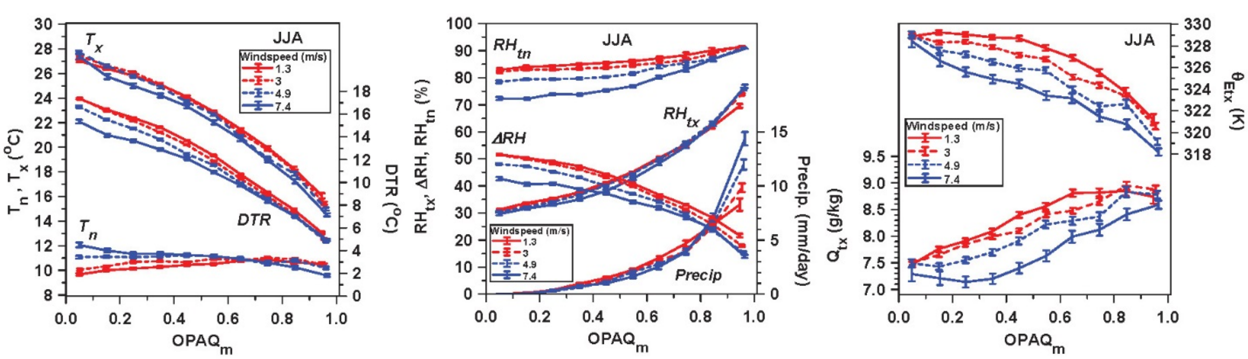

Figure 12: Coupling of $OPAQ_m$ and windspeed to diurnal cycle of temperature (left); (center) precipitation and diurnal cycle of RH, and (right) afternoon Q_{tx} and θ_{Etx} *(from Betts et al. 2015)*

Day and night radiative forcing by ECA and LW_n

The diurnal temperature range satisfies relationships to both daytime heating, where R_n is partitioned based on the availability of soilwater for evapotranspiration, and the night-time cooling by LW_n. Figure 13 shows the relationship between the diurnal temperature range and LW_n (left) and (right) ECA, both stratified by RH_m. The left panel shows that DTR, the cooling from afternoon T_x to sunrise T_n, has a nearly linear relationship to LW_n (Betts 2006; Betts et al. 2015).

$$DTR = 1.95(\pm 0.04) - 0.146(\pm 0.001)*LW_n \quad (R^2 = 0.61) \tag{10}$$

The value of $R^2 = 0.61$ for the linear regression fit to the daily data is high, considering that we have all the synoptic variability in 54000 days of data. Unlike Figure 11, DTR has no dependence on RH_m, even though LW_n itself does depend on RH_m (Figure 5). For T_x and T_n, we see a warm shift under dry conditions that would for example include droughts.

The right panel shows that the daytime forcing of DTR depends on RH_m as well as the solar forcing, represented here by ECA. DTR increases with decreasing cloud forcing and RH_m. One interpretation is to regard RH_m as the 'surface climate response' to the availability of soilwater for evapotranspiration, which determines the energy partition. The subgroup with low RH_m then represents dry soils, where sensible heat H is larger for the same R_n (which depends on ECA), giving a larger DTR. However a full understanding this fully coupled system requires a model for the growing daytime CBL.

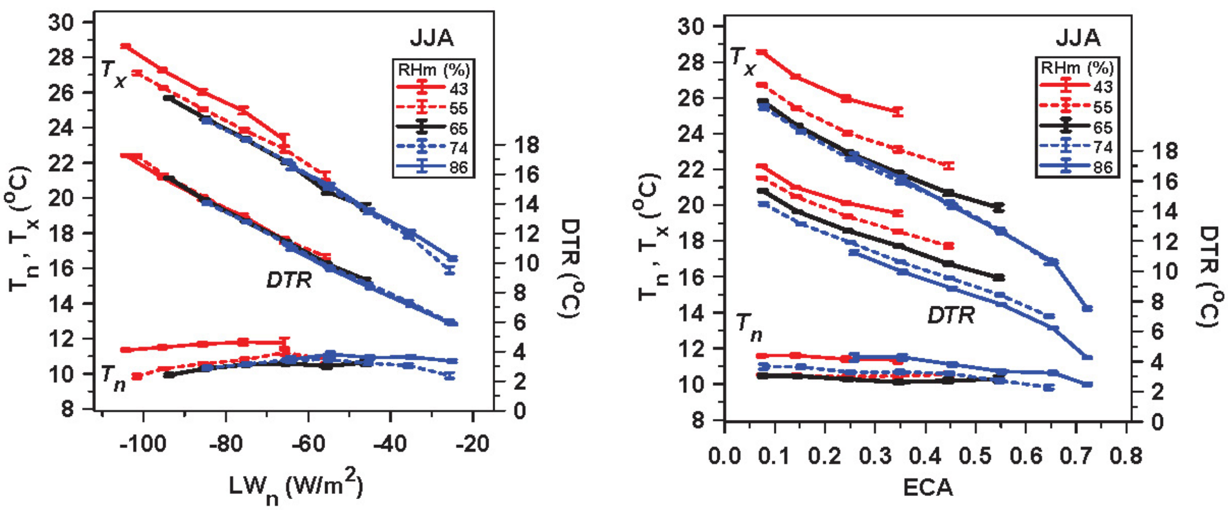

Figure 13. Coupling between diurnal temperature range and LW_n (left) and (right) ECA, stratified by RH_m.

Summary and conclusions

This research with the Canadian Prairie climate data is ongoing: future papers will be available at http://alanbetts.com. The availability of this 60-year hourly climate data set of such high quality, containing opaque, reflective cloud data that can be calibrated to give the SWCF and LWCF, has been transformative. For the first time we have a full set of data on climate time-scales for the coupled land-atmosphere-cloud system that will be invaluable for model evaluation, where the computed cloud radiative forcing has always been uncertain.

The warm and cold seasons are sharply delineated at northern latitudes by the freezing point of water, which determines whether precipitation falls as rain or snow. Surface snow cover on the Prairies acts as a fast climate switch that drops the air temperature by 10K within a few days, primarily by the increase in surface albedo from roughly 0.2 to 0.7. The surface-atmosphere-cloud coupling shifts with snow from a warm regime that is SWCF dominated to one that is LWCF dominated. The warm SWCF regime is characterized by a growing unstable convective BL, where afternoon T_x increases as cloud cover decreases. The cold LWCF regime with snow cover is characterized by a stable BL, where T_n before sunrise falls as cloud cover decreases. The rapidity of the shift between these two climate states with and without surface snow means that the cold season temperature depends on snow cover. In Alberta where the snow cover is more transient than in the central Prairies, about 80% of the variance of cold season mean temperature is related to the fraction of days with snow cover.

It is clear that hydrometeorology in the warm season requires understanding the differing impacts of both precipitation and cloud radiative forcing on temperature and RH. The cloud forcing dominates on the daily timescale, although the diurnal cycle impacts of other surface variables such as surface wind, RH (and precipitation anomalies, not shown here) can be readily seen. On monthly timescales, precipitation and cloud forcing impact both the mean and the diurnal cycle of temperature and humidity, which in turn gives the LCL and equivalent temperature that feedback on the probability of clouds and precipitation. The large shift in land-use on the Prairies in recent decades from summerfallow to continuous cropping shows how the growing season climate has been cooled and moistened by increased transpiration.

Acknowledgement

This research was supported by Dr. Ray Desjardins and Agriculture and Agri-Food Canada. We thank the civilian and military technicians of the Meteorological Service of Canada and the Canadian Forces Weather Service, who have made reliable cloud observations hourly for 60 years.

References

Beljaars, A.C.M., Viterbo, P., Miller, M.J., and Betts, A.K. (1996). The anomalous rainfall over the United States during July 1993: sensitivity to land surface parameterization and soil moisture anomalies. *Mon. Wea. Rev*., 124, 362-383.

Berg, A., B. R. Lintner, K. Findell, S. I. Seneviratne, B. van den Hurk, A. Ducharne, F. Chéruy, S. Hagemann, D. M. Lawence, S. Malyshev, A. Meier and P. Gentine (2014). Interannual Coupling between Summertime Surface Temperature and Precipitation over Land: Processes and Implications for Climate Change. *J. Climate*, 28, 1308-1328.

Betts, A. K. (2000). Idealized model for equilibrium boundary layer over land. *J. Hydrometeorol.,* 1, 507-523.

Betts, A. K., 2004. Understanding Hydrometeorology using global models. *Bull. Amer. Meteorol. Soc*., 85, 1673-1688. (AMS Robert E. Horton Lecture)

Betts, A. K. (2006). Radiative scaling of the nocturnal boundary layer and the diurnal temperature range, *J. Geophys. Res*., 111, D07105, doi:10.1029/2005JD006560.

Betts, A. K. (2007). Coupling of water vapor convergence, clouds, precipitation, and land-surface processes, *J. Geophys. Res*., 112, D10108, doi:10.1029/2006JD008191.

Betts, A. K. (2009). Land-surface-atmosphere coupling in observations and models. *J. Adv. Model Earth Syst.,* Vol. 1, Art. #4, 18 pp., doi: 10.3894/JAMES.2009.1.4

Betts, A.K. and Ball, J.H. (1995). The FIFE surface diurnal cycle climate. *J. Geophys. Res.* **100**, 25679-25693.

Betts A. K. and Ball, J. H. (1998). FIFE surface climate and site-average dataset: 1987-1989. *J. Atmos Sci* , **55,** 1091-1108.

Betts, A. K and Viterbo, P. (2005). Land-surface, boundary layer and cloud-field coupling over the south-western Amazon in ERA-40. *J. Geophys. Res*., 110, D14108, doi:10.1029/2004JD005702.

Betts, A.K. and A.B. Tawfik 2015. Annual climatology of the diurnal cycle on the Canadian Prairies. Submitted to Frontiers in Earth Science.

Betts, A. K., J.H. Ball, A.C.M. Beljaars, M.J. Miller and P. Viterbo, (1996). The land-surface-atmosphere interaction: a review based on observational and global modeling perspectives. *J. Geophys. Res.* 101, 7209-7225.

Betts, A.K., R. Desjardins and D. Worth (2013a). Cloud radiative forcing of the diurnal cycle climate of the Canadian Prairies. *J. Geophys. Res. Atmos.*, 118, 8935–8953, doi:10.1002/jgrd.50593.

Betts, A. K., R. Desjardins, D. Worth, and D. Cerkowniak (2013b). Impact of land use change on the diurnal cycle climate of the Canadian Prairies, *J. Geophys. Res. Atmos.*, 118, 11,996–12,011, doi:10.1002/2013JD020717.

Betts, A.K., R. Desjardins, D. Worth, S. Wang and J. Li (2014a). Coupling of winter climate transitions to snow and clouds over the Prairies. *J. Geophys. Res. Atmos*., 119, 1118-1139, doi:10.1002/2013JD021168.

Betts, A.K., R. Desjardins, D. Worth and B. Beckage (2014b). Climate coupling between temperature, humidity, precipitation and cloud cover over the Canadian Prairies. *J. Geophys. Res. Atmos*. 119, 13305-13326, doi:10.1002/2014JD022511.

Betts, A.K., R. Desjardins, A.C.M. Beljaars and A. Tawfik (2015). Observational study of land-surface-cloud-atmosphere coupling on daily timescales. *Front. Earth Sci. 3:13*. http://dx.doi.org/10.3389/feart.2015.00013

De Ridder, K. (1997). Land Surface Processes and the Potential for Convective Precipitation, *J. Geophys. Res.* 102, 30,085–30,090.

Flato, G., Marotzke, J., Abiodun, B., Braconnot, P., Chou, S.C., Collins, W., Cox, P., and Coauthors (2013). Evaluation of Climate Models. In: Climate Change 2013: The Physical Science Basis. Contribution of Working Group I to the Fifth Assessment Report of the Intergovernmental Panel on Climate Change [Stocker, T.F., D. Qin, G.-K. Plattner, M. Tignor, S.K. Allen, J. Boschung, A. Nauels, Xia, Y., Bex, V., and Midgley, P.M. (eds.)]. Cambridge University Press, Cambridge, United Kingdom and New York, NY, USA.

Gameda, S., B. Qian, C.A. Campbell and R.L. Desjardins (2007). Climatic trends associated with summerfallow in the Canadian Prairies. *Agric. Forest Meteorol*., 142, 170–185. doi:10.1016/j.agrformet.2006.03.026.

Koster, R. D. and Suarez, M. J. (2001). Soil moisture memory in climate models. *J. Hydrometeor.*, 2, 558–570.

MANOBS (2013). Environment Canada MANOBS, Chapter 1, Sky. [Available at http://www.ec.gc.ca/manobs/default.asp?lang=En&n=A1B2F73E-1].

Qian, B., X. Zhang, K. Chen, Y. Feng, and T. O'Brien (2009). Observed Long-Term Trends for conditions in Canada. *J. Appl. Meteorol. Climatol*., 49, 604-618. DOI: 10.1175/2009JAMC2275.1

Qian, B., S. Gameda, X. Zhang and R. De Jong (2012). Changing growing season observed in Canada. *Climatic Change,* 112, 339–353. DOI 10.1007/s10584-011-0220-8

Raddatz, R.L. (1998). Anthropogenic vegetation transformation and the potential for deep convection on the Canadian Prairies. *Can. J. Soil Sci.* 78, 657–666.

Raddatz, R.L.and J.D. Cummine (2003). Inter-annual variability of moisture flux from the Prairie agro-ecosystem: impact of crop phenology on the seasonal pattern of tornado days. *Boundary-Layer Meteorol.* 106, 283–295.

Schwartz, M.D. and T.R. Karl (1990). Spring Phenology: Nature's Experiment to Detect the Effect of "Green-Up" on Surface Maximum Temperatures. *Mon. Wea. Rev.,* 118, 883-890.

Schwartz, M. D. (1994). Monitoring global change with phenology: The case of the spring green wave. *Int. J. Biometeor.,* 38, 18–22.

Schwartz, M. D. (1996). Examining the spring discontinuity in daily temperature range. *J. Climate*, *9*, 803–808.

Wang, S., Y. Yang, Y. Luo, and A. Rivera (2013). Spatial and seasonal variations in evapotranspiration over Canada's landmass. *Hydrol. Earth Syst. Sci. Discuss.,* 10, 6107–6151. doi:10.5194/hessd-10-6107-2013 www.hydrol-earth-syst-sci-discuss.net/10/6107/2013/

ABOUT THE AUTHOR

Alan Betts: Dr. Alan Betts of Atmospheric research in Pittsford, Vermont, USA is an independent climate scientist. He is a Fellow of the American Geophysical Union, the American Meteorological Society (AMS), the Royal Meteorological Society, the American Association for the Advancement of Science, and a past-president of the Vermont Academy of Science and Engineering. He is the author or co-author of more than 165 reviewed papers in the scientific literature. He was the AMS Robert E. Horton Lecturer in Hydrology in 2004; and the AMS Jule Charney Award winner in 2007. His research, public lectures and articles are available at alanbetts.com.